Solar RRL
www.solar-rrl.com

Nickel and Cobalt Selenite Hydrates as Broad Solar Absorbers for Enhanced Solar Water Evaporation

Anastasiia Taranova, Edlind Lushaj, Kamran Akbar, Elena Ghedini, Isabel Barroso-Martín, Alessandro Gradone, Vittorio Morandi, Enrique Rodríguez-Castellón, Wenliang Zhu,* Elisa Moretti,* and Alberto Vomiero**

Inorganic black materials possessing hydrophilicity are scarce but can be of great importance in areas such as solar water evaporation and solar steam generation. Herein, for the first time, transition-metal selenite hydrates (specifically, Earth-abundant metals Ni and Co) not only possess high solar absorbance (>96 %) in the solar spectral range (UV–vis–NIR) but also excellent hydrophilicity, which plays a key role in water transport in the solar steam generation. The hydrophilic behavior in selenite hydrates originates from trapped "water of hydration" inside its crystal lattice, which can easily form hydrogen bonds with other water molecules, facilitating water transport. Owing to the abovementioned properties, the studied selenite hydrates are tested for solar water evaporation, showing excellent water evaporation rates of 1.83 and 2.34 kg m^{-2} h^{-1} for nickel selenite hydrate and cobalt selenite hydrate, exceeding the theoretical limit of 1.47 kg m^{-2} h^{-1}.

1. Introduction

Interfacial solar water evaporation is among the recently developed technologies aiming to secure fresh water supply for growing domestic and commercial needs.[1–3] A typical interfacial solar water evaporation system consists of a photothermal absorber layer placed on top of a thermal insulator to limit heat waste and a saline/polluted water reservoir that is connected to the absorber layer via water transport materials such as cotton and similar materials.[4] The sunlight illumination on the photothermal layer raises its temperature, which then converts the saline/polluted water into its vapors. These vapors are condensed back into liquid water to generate clean drinking water. To achieve a high water evaporation rate, photothermal materials must simultaneously exhibit broad solar absorption and efficient water transport.[5,6] Broad solar absorption in the spectral range (0.3–2.5 μm) allows full utilization of the entire available solar energy, while efficient water transport ensures a constant water supply to the evaporator. Typically, natural biomass-based materials, such as wood and certain polymeric hydrogels, provide efficient water transport due to their capillary action, excellent hydrophilicity, or both.[7–11] Capillary action is dependent on the size of micro-/nanoporous channels used to transport water, and hydrophilicity depends on the attachment of hydrophilic functional groups such as —OH and —COOH, which possess a high affinity toward water molecules.[7,8,11–13] Hydrogels and naturally occurring organic structures (such as wood) combine these properties and hence enhanced evaporation rates have been observed for these systems. These structures, despite their excellent hydrophilicity, lack intrinsic broad solar absorption and thus often require the assistance of black absorber materials to harvest light. For instance, Zhao et al.[6] developed a polyvinyl alcohol-based

A. Taranova, E. Lushaj, K. Akbar, E. Ghedini, E. Moretti, A. Vomiero
Department of Molecular Sciences and Nanosystems
Ca' Foscari University of Venice
Via Torino 155, 30172 Venezia Mestre, Italy
E-mail: kamran.akbar@unive.it; elisa.moretti@unive.it; alberto.vomiero@ltu.se

A. Taranova, W. Zhu
Ceramic Physics Laboratory
Kyoto Institute of Technology
Sakyo-ku, Matsugasaki, Kyoto 606–8585, Japan
E-mail: wlzhu@kit.ac.jp

E. Ghedini
INSTM RUVe
Via Torino 155, 30172 Venezia, Italy

I. Barroso-Martín, E. Rodríguez-Castellón
Department of Inorganic Chemistry
Faculty of Science
University of Málaga
29071 Málaga, Spain

A. Gradone, V. Morandi
CNR Institute for microelectronics and microsystems (IMM)
Via P. Gobetti 101, 40129 Bologna, Italy

A. Vomiero
Division of Materials Science
Department of Engineering Sciences and Mathematics
Luleå University of Technology
SE-971 87 Luleå, Sweden

The ORCID identification number(s) for the author(s) of this article can be found under https://doi.org/10.1002/solr.202400198.

DOI: 10.1002/solr.202400198

hydrogel structure that provides excellent hydrophilicity but poor solar absorption due to its transparent nature. It was combined with black absorber polypyrrole to attain the desired broad solar absorption. On the other hand, naturally occurring organic-based structures need carbonization at elevated temperatures to attain the desired broad intrinsic solar absorption. Further, these organic-based structures (including hydrogels) suffer bacterial fouling under real-world conditions, which severely limits their long-term use and practical applications.[14,15]

Despite the prevalence of organic-based structures, which possess excellent broad solar absorption (after carbonization) and the desired hydrophilicity, there is a significant void in inorganic-based structures possessing such properties. In particular, broad inorganic-based intrinsic solar absorbers with sufficient hydrophilicity are virtually nonexistent in the literature. In most cases, inorganic materials possess excellent broad absorption or good hydrophilicity, but it is difficult to find a combination of these two properties in a single material. For instance, various excellent hydrophilic inorganic materials such as zeolites, clays, and silica lack intrinsic broad solar absorption. However, their exceptional hydrophilic properties originate either from their nanoporous structure (e.g., zeolites) or due to their polarity, which allows the incorporation of water of hydration into their structures (such as clays and silica).[16] Using hydrates in solar water evaporators is a promising method to solve the global water crisis. Water molecules embedded in their crystal lattice make hydrate compounds unique and suitable for solar-driven water evaporation. Hydrates are an appealing solution for sustainable water desalination due to their remarkable efficiency, cost-effectiveness, and durability. The high efficiency of hydrates is a key benefit, as they can absorb substantial amounts of water vapor, resulting in optimal water evaporation for a given solar energy input. Furthermore, the low production costs of hydrates make them economical for large-scale applications. Their durability and ability to withstand harsh environmental conditions further enhance the appeal for widespread implementation. The focus of this article is on the scalability of hydrates, which have the potential to revolutionize water desalination systems and lead to a more sustainable and accessible water supply.

In this context, our research endeavors resulted in the development of Earth-abundant-based metal (Ni and Co) selenite hydrates (**Figure 1**). Exceptional hydrophobicity and broad solar absorption capabilities are both features of these innovative materials, which are exemplified by cobalt selenite hydrates (CoSe-hyd) and nickel selenite hydrate (NiSe-hyd). These properties have been integrated to generate a remarkable water evaporation rate, with observed values of 2.35 and 1.85 $kg\,m^{-2}\,h^{-1}$ for CoSe-hyd and NiSe-hyd samples, respectively. Our approach to create sustainable and scalable solutions for freshwater production will be made possible by combining efficient water transportation with broad solar absorption in the material. This innovative approach has great potential for addressing global water shortage challenges in the future.

2. Experimental Section

2.1. Materials and Methods

Ni selenite hydrate and cobalt selenite hydrate were prepared by aqueous synthesis. 10 mM of nickel(II) acetate (or cobalt(II) acetate) was dissolved in 50 mL of deionized water. NaHSe solution was obtained by dissolving 227 mg $NaBH_4$ in 50 mL deionized water with further addition of 237 mg of Se powder ($2Se + 4NaBH_4 + 7H_2O \rightarrow 2NaHSe + Na_2B_4O_7 + 14H_2\uparrow$). The solution Ni-acetate (or Co-acetate) was heated to 100 °C in the oil bath after injection of the fresh NaHSe solution. The mixture was boiled in the oil bath for 180 min. After cooling to room temperature, the products were collected by centrifugation, washed using ethanol and deionized water several times, and dried at 70 °C overnight. The fabrication of the membranes was performed through a vacuum filtration process. 50 mg of each powder was dissolved in 250 mL of deionized water in an ultrasonicated bath, and then deposited on a glass–wool microfiber filter paper with a diameter of absorber spot of 35 mm via vacuum filtration.

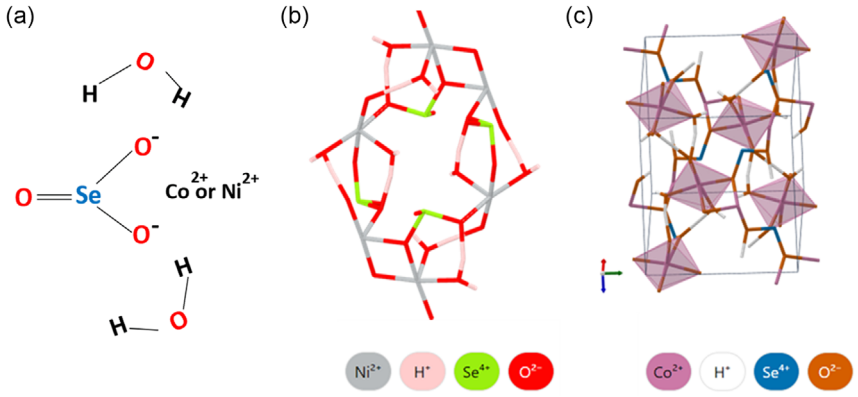

Figure 1. a) Chemical structural representation of cobalt- and nickel-based selenite hydrates showing the presence of water of hydration in the structure. b) Wireframe model of nickel selenite showing the presence of abundant OH groups. c) The crystalline structure of cobalt selenite (similar to nickel selenite). Both Ni and Cobalt selenite possess similar crystalline structures, but different representations in (b) and (c) are given to better visualize structural features.

2.2. Characterization

The crystalline structure of the samples was obtained using X-Ray diffraction (XRD) on a Philips PW1050/37 diffractometer using Cu K_α radiation ($\lambda = 1.5418$ Å), which was recorded over the angular range from 20° to 70° with the step of 0.05°. The specific surface area and pore-size distribution were determined by N_2 physisorption analysis at −196 °C using a Tristar 2 Plus (Micrometrics). Before the measurement, the samples were purified at 80 °C for 2 h with a vacuum degasser system. The calculation of surface area was done according to the Brunauer–Emmett–Teller method.[17,18] A FEI Tecnai F20 high-resolution transmission electron microscope (HRTEM), equipped with a Schottky transmitter operating at 200 kV, was used for the estimation of details on crystal structure, nanoscale morphology, and composition. The elemental analysis was carried out by energy-dispersive X-Ray spectroscopy (EDS), coupled with high-angle annular dark-field (HAADF) scanning transmission electron microscopy (STEM–HAADF) to map the elemental distribution. X-ray photoelectron spectroscopy (XPS) spectra of the samples were obtained to determine the chemical composition of the surface and the chemical state of the elements. The measurements were conducted on a PHI VersaProbe II Scanning XPS Microprobe with monochromatic X-Ray Al Kα radiation used as the excitation source (200 μm area analyzed, 52.8 W, 15 kV, 1486.6 eV). The pressure in the analysis chamber was maintained lower than $2.0 \cdot 10^{-6}$ Pa. High-resolution spectra of C 1*s*, O 1*s*, Co 2*p*, Ni 2*p*, and Se 3*d* were recorded at a given take-off angle of 45° by a multichannel hemispherical electron analyzer operating in the constant pass energy mode at 29.35 eV and the Au $4f_{7/2}$ line was recorded with 0.73 eV full width at half maximum (FWHM) at binding energy (BE) of 84.0 eV. BEs were corrected for charging by reference to the C 1*s* at 284.8 eV. The energy scale was calibrated using Cu $2p_{3/2}$, Ag $3d_{5/2}$, and Au $4f_{7/2}$ photoelectron lines at 932.7, 368.2, and 83.9 eV, respectively. The spectra were analyzed using PHI SmartSoft software and processed using MultiPak 9.3 package. Raman measurement was carried out on a dedicated Raman device (RAMANtouch, Nanophoton Co., Minoo, Osaka, Japan) operating in microscopic measurement mode (50× lens; numerical aperture, NA = 0.9). A 532 nm solid-state laser was used as the excitation source and the spectral pixel resolution was 0.3 cm^{-1} $pixel^{-1}$. Scanning electron microscopy (SEM) images were obtained using a SEM (JSM-7001 F, JEOL) operating at an accelerating voltage of 15 kV, equipped with EDS. Contact angle measurement for evaluating the wettability was conducted using Phoenix 300 Touch (SEO, South Korea) and software Surfaceware9. The rating adhesion test of the membrane was based on the procedure described in ASTM D3359–23.[19] The solar absorptance spectrum of compounds was measured using an ultraviolet-visible-near infrared (UV-Vis-NIR) spectrophotometer (LAMBDA 1050+, Perkin Elmer) equipped with an integrating sphere. For the IR spectral region, Fourier transform infrared (FTIR) spectrometer (Nicolet 6700 FT-IR Spectrometer) was used. The spectrally averaged solar absorptance $\overline{\alpha}$ and averaged thermal emissivity $\overline{\varepsilon}$ were defined by Equation (1) and (2).[20] The solar–thermal energy conversion efficiency η was calculated from Equation (3).[21]

$$\overline{\alpha} = \frac{\int_{0.3\mu m}^{2.5\mu m} \alpha(\lambda) E_{solar}(\lambda) d\lambda}{I_{solar}} \quad (1)$$

$$\overline{\varepsilon}(T) = \frac{\int_{0.3\mu m}^{20\mu m} \varepsilon(\lambda) E_b(\lambda, T) d\lambda}{\sigma \cdot T^4} \quad (2)$$

$$\eta(T) = \overline{\alpha} - \overline{\varepsilon} \frac{\sigma\left(T^4 - T_0^4\right)}{C \cdot I_{solar}} \quad (3)$$

where $E_{solar}(\lambda)$ is the spectral solar power (AM 1.5 G), I_{solar} is the total solar power density (1 sun, 1 kW m^{-2}), $\varepsilon(\lambda)$ is the emissivity at the wavelength λ, $E_b(\lambda,T)$ is the spectral irradiance of a blackbody at T the operating temperature, σ is the Stefan–Boltzmann constant ($5.6696 \cdot 10^{-8}$ W m^{-2} K^{-4}), C is concentration ratio, and T_0 is the ambient temperature.

2.3. Solar Water Evaporation

The solar water evaporation experiments were carried out using a solar simulator (Abet Technologies model 10 500) with output-simulated solar flux at 1 sun (AM 1.5 G, 100 mW cm^{-2}), with a 3 cm-diameter light spot. The simulated solar flux at 1 sun was calibrated with a Si standard solar cell. The setup of the solar vapor evaporation measurements (see the scheme in **Figure 2**a) consisted of a glass beaker (55 mm height with an inner diameter of 32.5 mm) fit with a thermal insulator (styrofoam) with a hole in the middle. The hole was filled with a water-absorbing cotton stick with a height of 6 cm. During the solar vapor generation process, the beaker contained 30 mL of simulated seawater (0.6 mol L^{-1} NaCl solution in the deionized water as 3.5 wt% average global seawater salinity). The membrane with the size 1 cm × 1 cm was placed on top of the cotton and irradiated with simulated sunlight. Photothermal behavior was tested for both dry (empty breaker) and wet conditions (when the beaker was filled with saline water). The evaporation mass loss of the receiver was monitored in the dark and under solar illumination 1 sun for 120 min by an Ohaus E1RR80 Explorer analytical balance with 0.1 mg resolution. Water evaporation experiments were carried out at a room temperature of (24 ± 1) °C and air humidity of ≈60%. The evaporation rate E (kg m^{-2} h^{-1}) was calculated according to Equation (4).[22]

$$E = \frac{\Delta m}{S \cdot \tau} \quad (4)$$

where Δm is the mass loss of water (kg), S is the area of the evaporation (m^2), and τ is the evaporation time (h).

To estimate the surface temperature, IR images of the membranes under solar illumination were taken by an IR camera (FLIR C3-X). The output temperature of the IR camera was calibrated to ensure accurate measurement of the surface temperature during the various temperature measurements reported in the study. For this purpose, the temperature measured by a thermocouple integrated into a hotplate and the temperature read by the thermal camera pointing at the surface of the hotplate were simultaneously acquired in the temperature range 30–110 °C. The investigated range was chosen to include the characteristic temperatures considered in the experiments and to guarantee the accuracy of the measurements under different conditions.

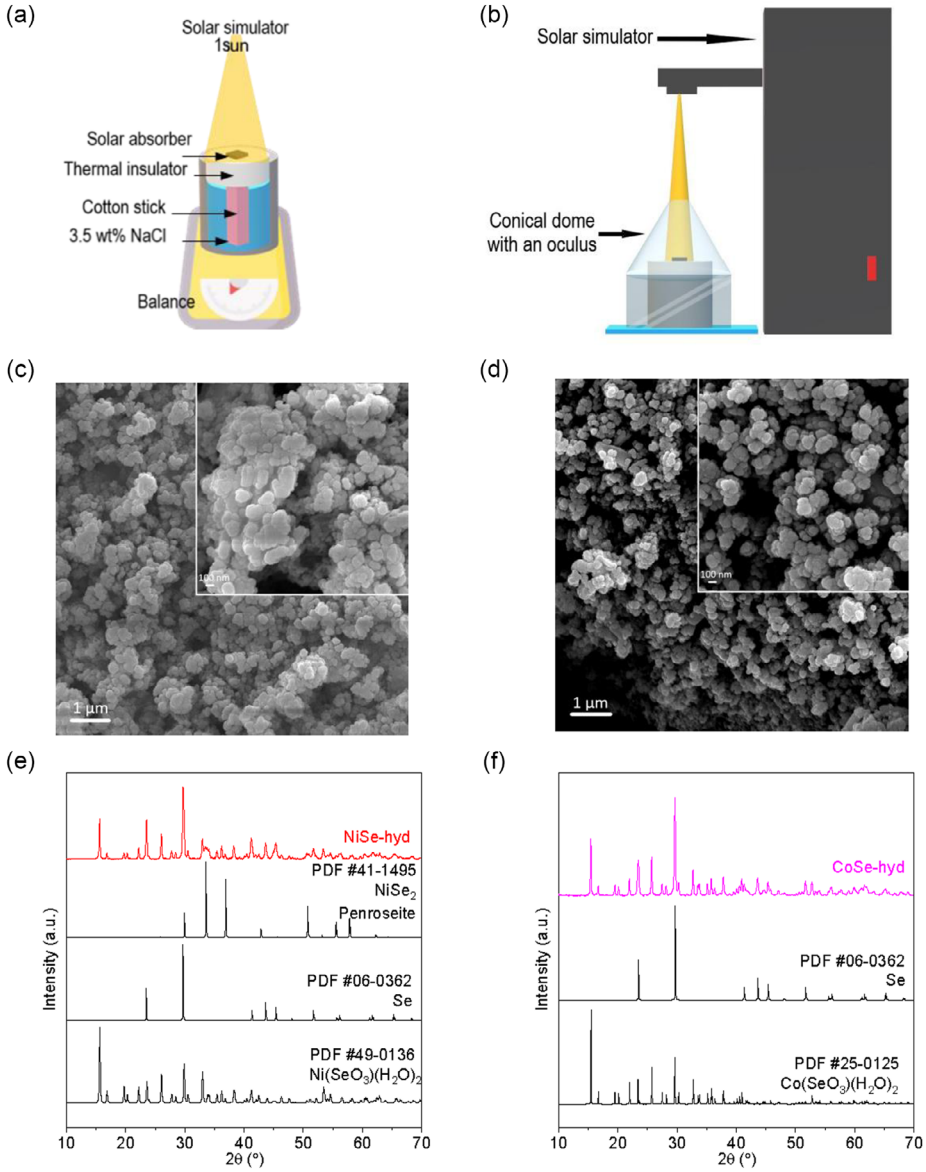

Figure 2. a) Schematic illustration of solar vapor generation test under 1 sun. b) Schematic illustration of setup for condensing the vapor. SEM images of c) NiSe-hyd and d) CoSe-hyd samples. High-magnification images are reported in the insets. XRD pattern of e) NiSe-hyd and f) CoSe-hyd samples. The PDF cards of the relevant phases are also reported.

To evaluate biological toxicity, the vapor underwent elemental analysis using microwave plasma atomic emission spectroscopy (MP-AES 4210, Agilent, USA) with a detection limit of 15 µg L^{-1} for cobalt and 20 µg L^{-1} for nickel. The setup for condensing the vapor is depicted in Figure 2b. A glass conical dome was placed on the beaker with the membrane. During the evaporation test, the steam condensed on the dome walls, and droplets flowed to the glass substrate for further collection of the condensed vapor (4 mL).

3. Results and Discussion

The low- and high-magnification SEM images of NiSe-hyd (c) and CoSe-hyd (d) in Figure 2 revealed that both samples are composed of small homogeneous aggregates, consisting of particles with a size of around 100 nm. Figure 2e demonstrates representative XRD patterns of NiSe-hyd, from which three crystalline phases can be detected. The main diffraction peaks centered at $2\theta = 23.53$, 29.70, and 43.86° correspond to the planes (100), (101), and (012) of metallic Se (PDF#06-0362). The peak at 33.33° is correlated to the crystalline phase of $NiSe_2$ (PDF#41-1495). The peak at 15.60° is attributed to reflections from the (011) plane, related to the ahlfeldite structure with the monoclinic phase of $NiSeO_3(H_2O)_2$ (PDF#49-0136). The broadness of the most intense peak at ≈29.75° is the result of the contribution of the phases discussed above. According to the Rietveld refinement, the contents of $NiSe_2$, Se, and $NiSeO_3(H_2O)_2$ are 2.7%, 26.6%, and 70.7%, respectively. From

the XRD pattern of the CoSe-hyd in Figure 2f, the strong peak at $2\theta = 15.44°$ can be assigned to the (011) plane of the monoclinic $CoSeO_3(H_2O)_2$ (PDF#25-0125), while the most intensive peak at ≈29.65° is the combination of two phases, $CoSeO_3(H_2O)_2$ and metallic Se (PDF#06-0362). Based on the Rietveld refinement the amounts of $CoSeO_3(H_2O)_2$ and Se were estimated as 73.9% and 26.1%, respectively. Low values of pore volume and surface areas of 43.8 and 40.8 $m^2 g^{-1}$ for NiSe-hyd and CoSe-hyd, respectively, were observed.

Transmission electron microscopy (TEM) analysis was performed to evaluate the crystalline structure and micro-/nanoscale morphology more in detail. **Figure 3** displays low- (a) and high-magnifications (b) images of nickel- and cobalt-based samples, respectively. The NiSe-hyd sample displayed two different types of structures, enclosed in a micrometer-sized aggregate. The first appears as flakes of different sizes with an elongated shape, attached to the other structure, represented by a more compact and homogenous phase. The TEM micrographs of CoSe-hyd (Figure 3b) showed that the sample displays micrometer-sized aggregates characterized by a not well-defined morphology. The microstructure is composed of many flakes of different sizes and shapes that give almost the same contrast, held together, or superimposed on each other.

To better understand the crystalline nature of the system under observation, selected-area electron diffraction (SAED) analyses were carried out. Both the SAED pattern of NiSe-hyd (Figure 3c) and CoSe-hyd (Figure 3d) display a polycrystalline structure, due to the aggregation of many crystallites of different dimensions and orientations, in agreement with TEM observations. From Figure 3c, the presence of some intense spots probably due to a greater crystalline domain can be observed. The *d*-spacings of the penroseite phase ($NiSe_2$) were recognized for NiSe-hyd and typical *d*-spacings of the trogtalite phase ($CoSe_2$) were also recognized.[23] However, the XRD analysis did not find the presence of the $CoSe_2$ phase, indicating a negligible amount of the trogtalite phase mixed with the most relevant cobalt selenite structure.

HRTEM micrographs allow for deeper analysis of nanometric flakes. Figure 3e shows that the crystalline character of NiSe-hyd matches that observed with SAED. The largest crystallites visible in the high-magnification image (red arrow) can be attributed to the one observed in the SAED with the brighter spots, while the smaller particles with a diameter between 1 and 3 nm were dispersed in an amorphous phase. The larger crystallites have the same nature as the nanoparticles, and they may emerge from a coalescence process. From the HRTEM image of CoSe-hyd

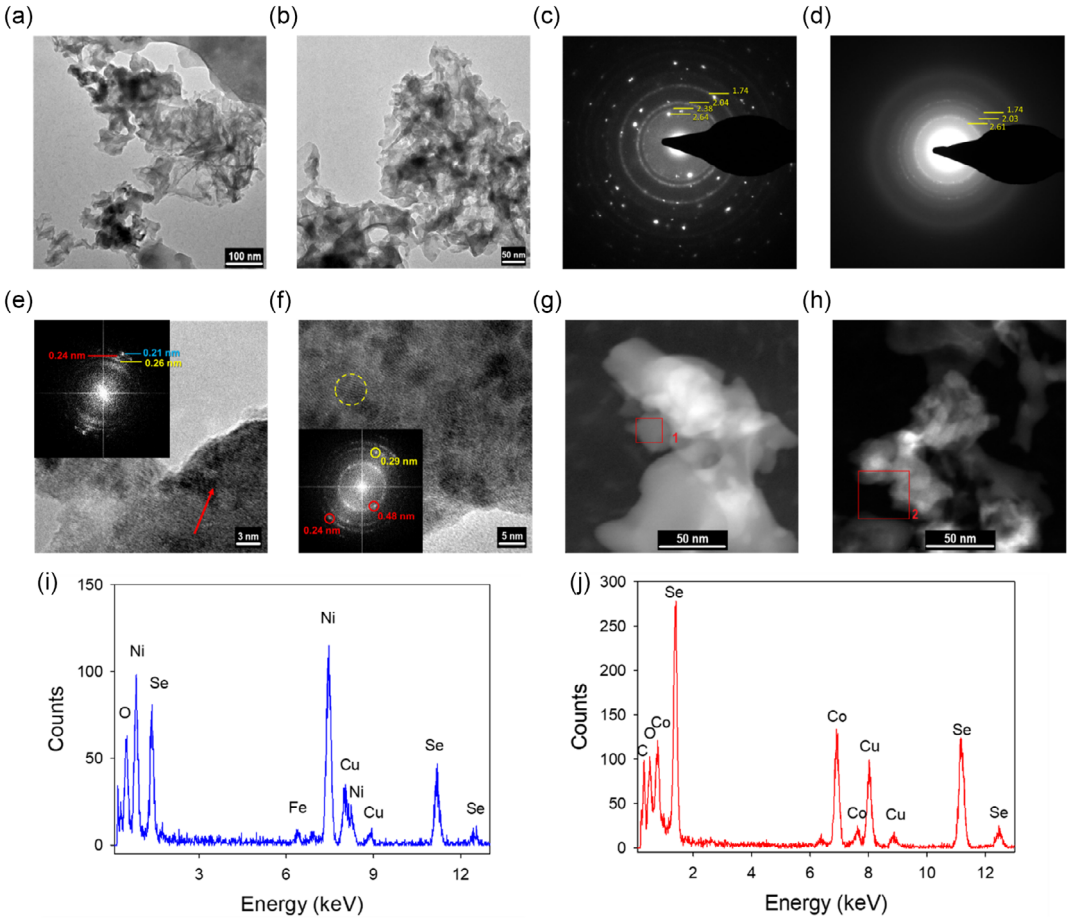

Figure 3. TEM images, SAED pattern, HRTEM micrograph, and HAADF–STEM micrograph of a,c,e,g) NiSe-hyd and b,d,f,h) CoSe-hyd. EDS positions analysis of i) NiSe-hyd and j) CoSe-hyd, taking into account the HAADF–STEM micrograph (g) and (h) as reference.

(Figure 3f), it is possible to highlight the presence of several nanoparticles with an average diameter of around 5 nm, randomly arranged and dispersed in an amorphous phase. The crystal fringes visible in the high-magnification images and highlighted in the fast fourier transform (FFT) inserts can be attributed to a trogtalite phase of $CoSe_2$, mostly thanks to the 0.24 nm distance that represents a fingerprint for this kind of structural arrangement of cobalt selenide. It should of course be noted that such analyses represent only a very small part of the sample, thus being less reliable than XRD analyses to highlight the crystalline composition in its entirety.

The nickel-based sample has been collected taking into account the HAADF–STEM micrograph as reference, as shown in Figure 3g,h. The spectra of NiSe-hyd (Figure 3i) display the presence of nickel and selenium, with a value in Ni/Se ratio that is slightly higher than what would be expected, in addition to a high value in the oxygen content. This result, which is in agreement with XRD data, indicates the presence of a nickel oxide structure that comes from the amorphous phase in which the smaller nanoparticles are dispersed, as observed in the high-resolution micrographs. The same scenario occurs in the case of CoSe-hyd sample. The EDS spectra for the CoSe-hyd sample (Figure 3j) display the presence of cobalt and selenium in addition to a high value in oxygen content. The Co atomic percentage is higher than what is expected in comparison with the Se content. This value combined with the O peak indicates the presence of a cobalt oxide structure that comes from the amorphous phase. These observations suggest that the majority component of the selenite-based sample is partly amorphous and acts as a matrix for the crystalline structures of a selenide phase.

XPS measurements were performed to study the surface chemical composition and environment of the prepared samples. **Figure 4**a shows the high-resolution XPS survey spectra of the NiSe-hyd and CoSe-hyd with the main peaks associated with the presence of carbon, oxygen, nickel, cobalt and selenium. Minimal amounts of sodium and boron were detected since $NaBH_4$ was used during the synthesis, and high-resolution spectra for these elements have not been included. From high-resolution spectra, semiquantitative analysis was performed, weight percentages were calculated, and relative atomic ratios are shown in **Table 1**. Based on it, NiSe-hyd has a higher metallic fraction in composition than CoSe-hyd, the ratio Ni/Se is almost doubled that Co/Se. The findings are also supported by XRD findings.

High-resolution C 1*s* core-level spectra were registered considering the adventitious carbon from the atmospheric contamination layer. Likewise, high-resolution O 1*s* core-level spectra were also recorded and the deconvoluted signals for both elements are shown in Figure 4b,c. Regarding the high-resolution C 1*s* spectra, both samples presented three contributions: the main one, around 284.8 eV, is associated with C—C and —C=C— bonds in adventitious carbon; the second one at ≈286 eV is related to C—OH or C—O—C bonds, and, finally, the contribution at highest BE 288.8 eV is attributed to carboxylate or carbonate species.[24,25] Concerning the high-resolution O 1*s* core-level spectra of all samples, these were deconvoluted into two contributions, at ≈530.8 and 532.2 eV, associated with lattice metal–oxygen bonds and superficial hydroxyl groups and chemisorbed oxygen, respectively, which is reasonable considering the hydrate sample formulation.[26,27]

High-resolution Co 2*p*, Ni 2*p*, and Se 3*d* core-level spectra were also recorded to study the different species present in these nanomaterials. As for Ni, Figure 4d shows the high-resolution Ni 2*p* core-level spectra. For NiSe-hyd samples, the registered signals were fitted considering the contributions at lower BE, ≈853.3 and 872 eV (Ni $2p_{3/2}$ and Ni $2p_{1/2}$), which have been reported as metallic Ni but also as Ni—Se bonds.[28,29] The stronger peaks located at around 856 and 874 eV are attributed to the Ni—O bond in the main component $NiSeO_3(H_2O)_2$. Figure 4e shows the Co 2*p* spectra for CoSe-hyd sample. CoSe-hyd presented six well-defined contributions. The one located at the lowest BE, 778.7 eV could be attributed to the Co $2p_{3/2}$ peak for CoSe which is supported by its doublet at ≈15 eV difference. The second contribution at 780.9 eV is associated with Co $2p_{3/2}$ of the Co^{2+} species binding to O (its Co $2p_{1/2}$ doublet at 797.1 eV).[30,31] The larger energy split between leading peaks in comparison with CoSe ones corroborates the coexistence of both CoSe and Co^{2+} species, which has been reported as Co—Se bonds in similar CoSe-hyd systems.[32–34] Finally, contributions at 785.0 and 802.4 eV are related to shake-up satellite peaks.[35] Figure 4f displays high-resolution Se 3*d* core-level spectra. In both samples, the Se $3d_{5/2}$ and Se $3d_{3/2}$ peaks are located at ≈54.3 and 55.4 eV, respectively, indicating the presence of Se—Se and Ni—Se (Co–Se) bonds, as the latter also observed in the Ni and Co spectra.[28,36,37] Likewise, a third contribution at around 59 eV was fit in both cases and ascribed to Se^{4+}, which is similar to the values of Se—O bond in SeO_3^{2-}.[38,39]

Figure 5 shows the Raman spectra of NiSe-hyd (a) and CoSe-hyd (b) under the irradiation of a 532 nm laser. Both samples show quite similar spectral morphologies, as two main intense peaks can be clearly observed: The peak located at ≈825 cm^{-1} for the NiSe-hyd sample (819 cm^{-1} for CoSe-hyd) is attributed to the symmetric stretching of $(SeO_3)^{2-}$ in $NiSeO_3(H_2O)_2$ (and $CoSeO_3(H_2O)_2$), while the peak located at ≈246 cm^{-1} (245 cm^{-1} for CoSe-hyd) originates from the stretching of Se—Se bond in metallic Se. Note that because of the nanosize of the particles, an agglomeration of the particles as well as a change in the particle size can cause a broadening and shift of the Raman bands. The results are in good agreement with those obtained from XRD and XPS analyses.

From the cross-section SEM image of the NiSe-hyd membrane presented in **Figure 6**a, the thickness of the photothermal layer was measured as 29 μm. We expect similar thickness for the membrane fabricated using the CoSe-hyd sample with the same amount of powder, given that the particle size for the two powders is similar. The water transfer capacity of NiSe-hyd and CoSe-hyd membranes was characterized by measuring the contact angle with water, the timelapse snapshots of which are illustrated in Figure 6b,c. Using the automatic evaluation features of the software, it was estimated that a drop of water with a volume of 5 μL was fully absorbed within 219 and 263 ms for NiSe-hyd and CoSe-hyd membranes, respectively, and a water contact angle of 58° for NiSe-hyd and 38° for CoSe-hyd was observed after 10 and 7 ms, respectively. The very fast water absorption of photothermal membranes indicated their superhydrophilicity due to the hydrophilic nature of both the glass–wool membrane and the selective absorber. Since the thickness of the membrane (glass–wool paper + powder) exceeds 125 μm, the rating of the adhesion of the membrane was based on the Method

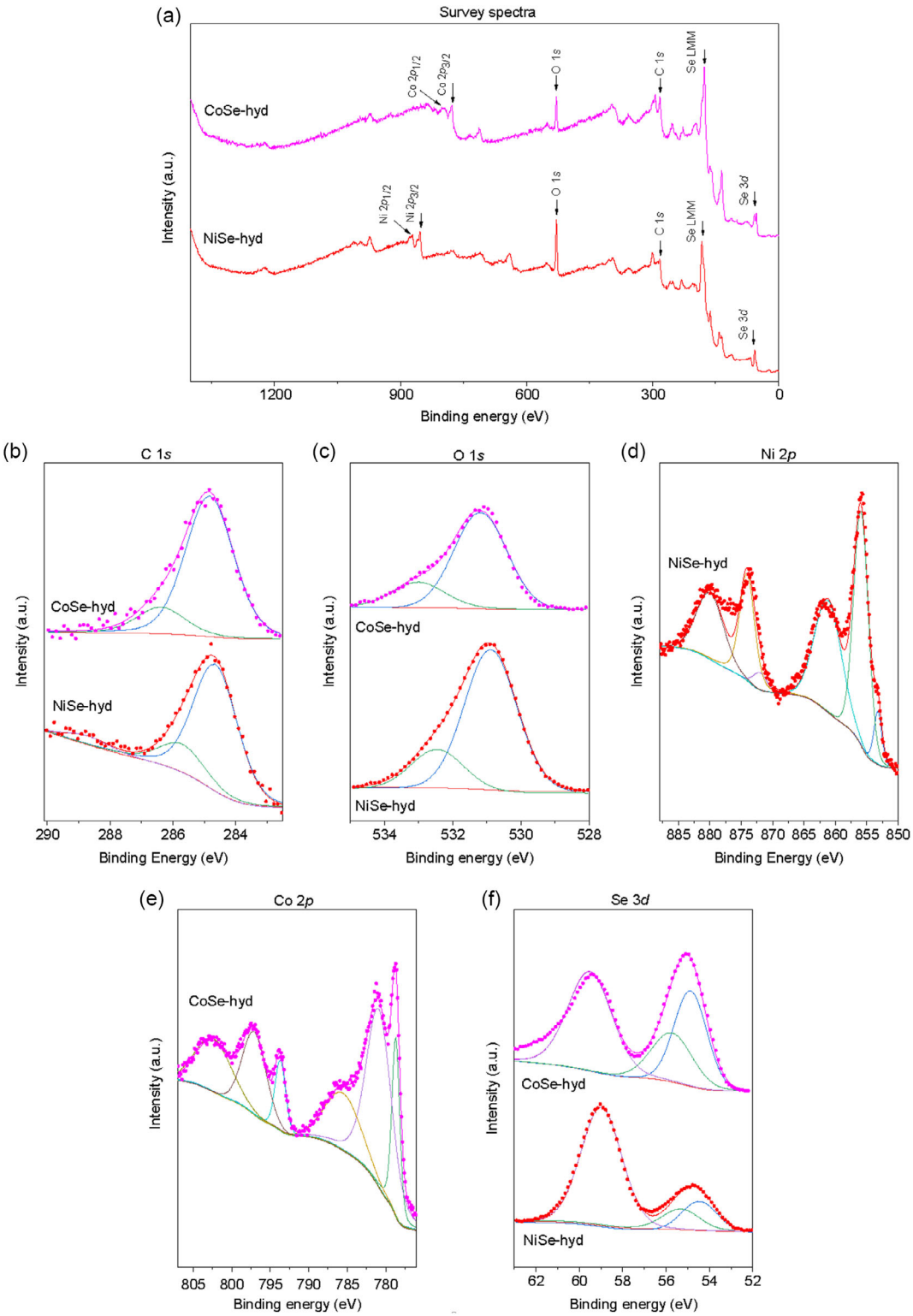

Figure 4. a) XPS survey spectra of NiSe-hyd and CoSe-hyd. Core level spectra for all prepared samples b) C 1*s*, c) O 1*s*, d) Ni 2*p*, e) Co 2*p*, and f) Se 3*d*.

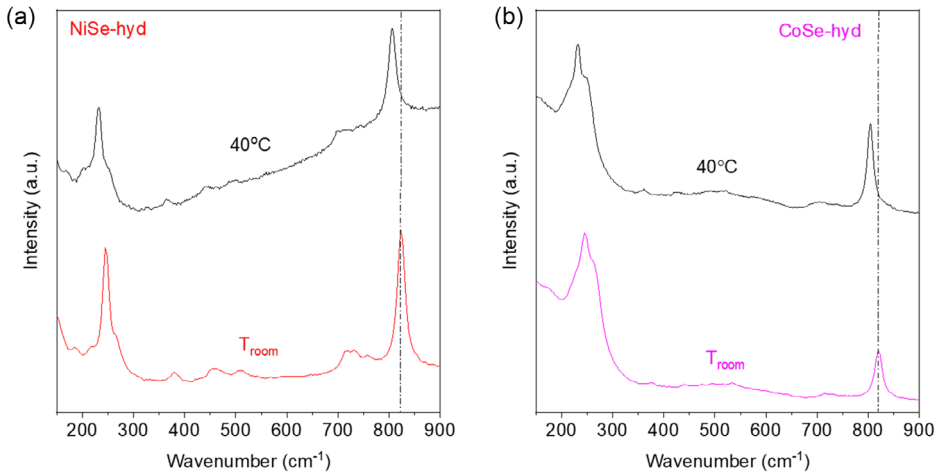

Figure 5. Raman spectra of a) NiSe-hyd and b) CoSe-hyd.

Table 1. Semiquantitative analysis of NiSe-hyd and CoSe-hyd.

Catalyst	wt%		Atomic ratio M/Se
	Se	M (M = Ni, Co]	
CoSe-hyd	51.85	16.06	0.41
NiSe-hyd	35.73	18.58	0.70

A—X-cut tape test.[19] The adhesion test requires the use of a sharp blade to create an X-cut in the coating. Subsequently, the pressure-sensitive adhesive tape is firmly applied to eliminate any poorly attached coating. Figure 6d illustrates the surface detachment test, displaying the precut membrane surface, the surface after the X-cut, and the membrane surface after the first, second, and third peeling stages. Based on the observed damages, the blade caused peeling along the incision and intersection (4A). After the first tape removal, the membrane was assessed using the "Classification of Adhesion Test Results for Test Method A" from ASTM D3359–23. The membrane was classified as 2A, indicating jagged removal along most of the incisions on both sides. During the second tape removal, most of the X area was eliminated (1A), and the third tape caused powder removal beyond the X-cut area (0A). The surface detachment test results underscore the stability of the membrane, despite the fabrication of the membrane without the use of any adhesion agent.

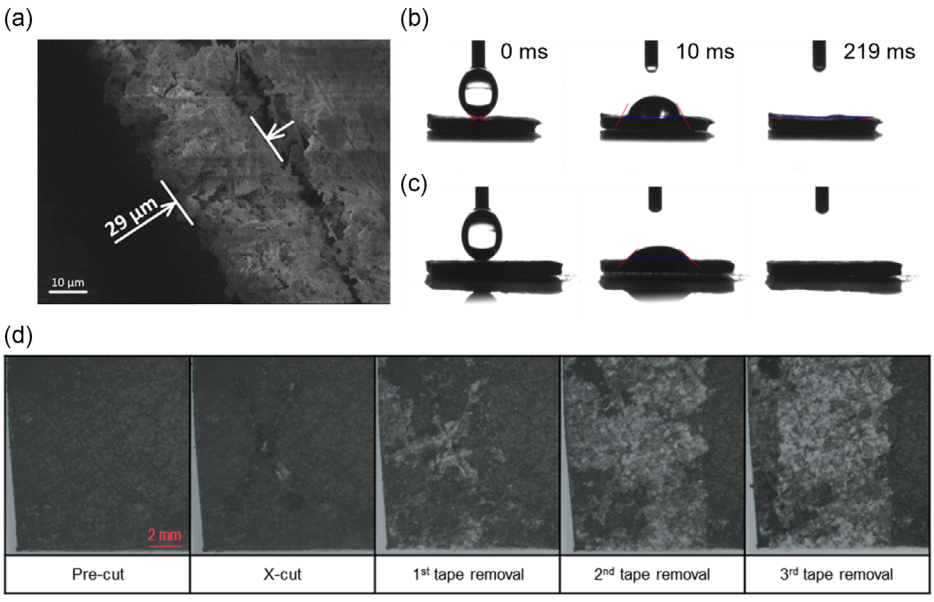

Figure 6. a) Cross-sectional SEM image of the NiSe-hyd membrane. Timelapse snapshots of absorbing a water droplet by the photothermal b) NiSe-hyd and c) CoSe-hyd membranes. d) Surface detachment test: the precut membrane surface, the surface after the X-cut, and the membrane surface after the first, second, and third peeling off stages.

Additionally, further incorporating adhesion promoters has the potential to enhance the bonding between the coating powder and the glass–wool substrate.

To investigate the photothermal behavior of the absorbers, a dry test was conducted. Given that both samples incorporate metallic selenium in their composition, an additional investigation of its contribution was undertaken by conducting the test under the membrane with 50 mg of selenium powder (Sigma-Aldrich, 100 mesh, ≥99.5%). The infrared images and temperature–time graph of the dry membranes under 1 sun irradiation are shown in **Figure 7**a,b. The surface temperature of CoSe-hyd increased rapidly and reached an equilibrium value of 67 °C within 3 min of illumination. NiSe-hyd membrane possessed a lower equilibrium temperature on the surface and reached 57 °C within 10 min. It is noteworthy that the surface temperature of the selenium membrane reached ≈41 ± 2 °C after 1.5 min and remained stable thereafter. Consequently, the observed photothermal effect characterized by the high surface temperature of NiSe-hyd and CoSe-hyd membranes can be attributed to the light absorption properties of transition-metal selenite hydrates. To ascertain the photophysical properties of NiSe-hyd and CoSe-hyd, the absorptances toward UV-Vis-NIR and emittance are presented in Figure 7c,d, respectively. CoSe-hyd exhibits an intense and broad absorptance of 97.5%, while NiSe-hyd exhibits 96.4% in the range of 0.3–2.3 μm. The broad intrinsic absorptance was extended into the NIR

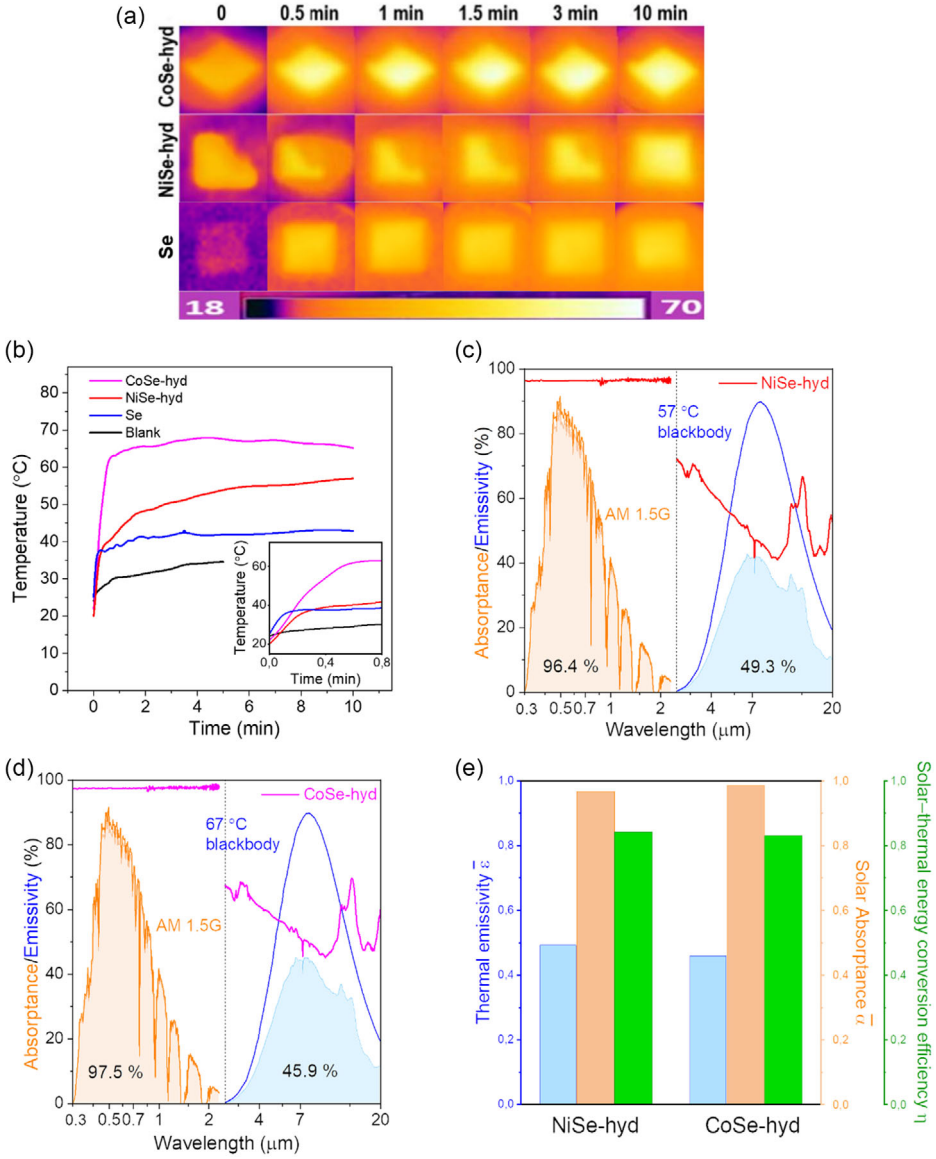

Figure 7. a) Timelapse IR images and b) photothermal behavior of NiSe-hyd, CoSe-hyd, and Se membranes under 1 sun in a dry state. Absorptance/emissivity spectra of c) NiSe-hyd and d) CoSe-hyd, as well as the AM 1.5G solar spectrum (orange) and the radiation spectrum of blackbody at 57 and 67 °C (blue). These two temperatures were chosen as the temperatures reached under simulated sun illumination in dry conditions. e) The bar graph of spectrally averaged solar absorptance $\bar{\alpha}$, averaged thermal emissivity $\bar{\varepsilon}$, and solar-to-thermal energy conversion efficiency.

region, ensuring complete energy harvesting from the entire solar spectrum. Simultaneously, the emissivity of the studied sample reaches around 50% in the IR region. Based on this, the spectral selectivity ($\overline{\alpha}/\overline{\varepsilon}$) of 1.96 and 2.12 for NiSe-hyd and CoSe-hyd, respectively, was obtained. Based on the XPS analysis results, the NiSe-hyd sample exhibits a significantly higher content of the metal phase. This is reflected in the UV–vis–NIR measurements, showing lower absorptance and higher emittance for NiSe-hyd compared to CoSe-hyd. From the values of $\overline{\alpha}$ and $\overline{\varepsilon}$, a normal-incidence solar–thermal conversion efficiency η of around 80% can be derived for both samples, which is presented in Figure 7e. Further improvement in spectral selectivity and solar absorption efficiency is crucial to enhance energy absorption and minimize energy losses due to reflection, reemission, and transmission.

Solar evaporation of seawater was carried out on NiSe-hyd and CoSe-hyd membranes under 1 sun for 2 h to demonstrate the potential for practical seawater desalination and the outstanding stability of the evaporation rate was estimated. The timelapse of the IR images of the surface temperature during solar water evaporation is presented in **Figure 8**a.

From the temperature–time graph in Figure 8b, the NiSe-hyd membrane reached an equilibrium temperature of 30 °C in around 20 min, while the CoSe-hyd membrane showed a stable temperature of 32 °C in 14 min.

From Figure 8c, the water evaporation rate for CoSe-hyd membrane showed 2.34 kg m^{-2} h^{-1} while NiSe-hyd demonstrated 1.83 kg m^{-2} h^{-1}, the values are above 5.3 and 4.2 times the evaporation rate of the blank membrane (glass–wool membrane without absorber layer) under 1 sun. The Se membrane was also tested and the evaporation rate of 1.48 kg m^{-2} h^{-1} was yielded.

Both materials maintain their physical–chemical features because the evaporation rate curve is parallel to the *x*-axis (time). The high evaporation rate values exceed the maximum theoretical limit of 1.47 kg m^{-2} h^{-1} (assuming a solar-to-vapor energy transfer efficiency of 100% under 1 sun irradiation) in case all incident energy is converted into solar-to-vapor generation.[1] The dark-condition evaporation rate (evaporation without illumination) of the NiSe-hyd and CoSe-hyd membranes was measured to be 0.40 and 0.49 kg m^{-2} h^{-1} and the linear trend after 1 h was estimated, reaching a stationary condition and yielding net evaporation rates of 1.43 and 1.85 kg m^{-2} h^{-1}.

The higher evaporation rate of CoSe-hyd compared to NiSe-hyd is due to several factors, such as a higher UV-Vis-NIR absorption, a higher surface temperature, the existence of a higher percentage of hydrate, and a lower amount of impurities estimated with Rietveld refinement. Nonetheless, both samples showed enhanced evaporation rates compared to previously reported inorganic materials, presented in **Table 2**. It is noteworthy that most of the mentioned solar evaporators have a 3D porous configuration with an artificially enhanced evaporation rate, they are relatively expensive in synthesis and installation compared with flat-plate solar water evaporators. By further improving the design of NiSe-hyd and CoSe-hyd by modifying it into 3D model, which harvests additional energy from the air and bulk water to enhance the evaporation rate, the values of the evaporation rate could overcome the reported ones. This is due to the excellent hydrophilicity, superior water transport, offered by NiSe-hyd and CoSe-hyd, and high light absorption efficiency. The upper water transport originates from the present water of hydration within these selenite hydrates. The presence of water within the structure can form hydrogen bonds

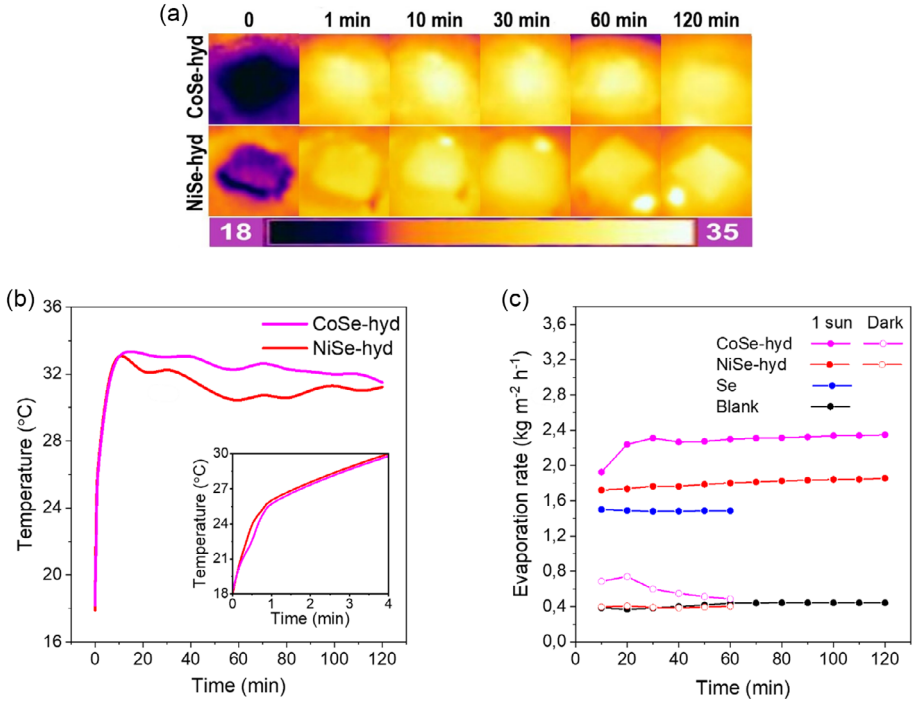

Figure 8. Timelapse a) IR images and b) photothermal behavior of NiSe-hyd and CoSe-hyd membranes under 1 sun during a water evaporation test. c) Evaporation rate of the membranes under 1 sun irradiation and in the dark.

Table 2. Comparison of intrinsic inorganic solar absorbers and their evaporation rates and hydrophilic properties.

Inorganic solar absorber	Absorption in UV–vis–NIR	Hydrophilicity, type, reason	Evaporation rate [kg m^{-2} h^{-1}]	Ref
Porous polydimethylsiloxane/Cu_7S_4-MoS_2-Au	+	+ 3D porous structure	3.82	[47]
Graphene/MoS_2 aerogel	+	+ 3D porous structure	3.2	[12]
Graphene/reduced Graphene oxide	+	+ OH functional group on GO 3D porous structure	2.39	[48]
Carbonaceous nanosheets/MXene foam		+ 3D porous structure OH functional group on MXene foam	1.39	[49]
MXene/PVA modified cellulose acetate fiber-based cigarette filters	+	+ 3D structure quasi-directional porous structures of cigarette filters OH functional group on MXene foam	3.38	[50]
Cu@CuO_2 foam/polydopamine	+	+ Cu foam morphology	1.58	[51]
Pr-doped Bi_2Se_3 nanosheets	+	–	1.66	[52]
Hydroxyapatite nanowires/NiO photothermal paper	+	Janus-type 2D	1.37	[53]
Polydopamine coated nickel-cobalt bimetal (Ni_1Co_3@PDA) nanosheet	+	+ 3D porous structure	2.42	[54]
Co-NCNT/NF (nitrogen-doped carbon nanotube@Co arrays are in situ grown on three-dimensional macroporous nickel foam)	+	– (dry) + (pre-wetted) 3D hierarchically porous configuration	1.65	[55]
SSA-Ni film (nickel nanoparticles are encapsulated in silica and carbon nanoshells)	+	2D Solar selective absorber	1.52	[56]
Ni_3S_2/NF (Ni_3S_2 nanosheet arrays/nickel foam)	+	+ 2D	1.29	[57]
Fumed silica with suspension concentration of 25 mg L^{-1}	+	+ Single-stage distillation (SSD) device	1.33	[58]
Natural wood-derived all-carbon conductive foam (ACCF)	+	+ 3D microporous structure Reduced evaporation enthalpy 2 V voltage	2.25	[59]
Au@Ag-Pd trimetallic nanostructure/polystyrene microsphere	+	Janus structures	3.04	[60]
Wood-inspired bimodal evaporator	+	+ 3D porous structure Low vaporization enthalpy	3.02	[61]
Ag/$MgFe_2O_4$@surface carbonized wood	+	+ 3D porous structure	1.55	[62]
Carbonized white gourd	+	+ Highly interconnected channels 3D porous structure	1.76	[63]
PVA hydrogel-Polydopamine/carbon black	+	+/– Vertically aligned channels 3D	1.73	[64]
Waste masks coated with a paste containing hydrophobic carbon black – polyvinylidene fluoride	+	– 2D	1.58	[65]
Carbon fiber cloth-based water diode	+	Janus structures 2D	2.14	[66]
NiSe-hyd	+	+ Hydrate in the content	1.83	This work
CoSe-hyd	+	+ Hydrate in the content	2.34	This work

with other water molecules coming from the water source and decreased energy requirements (reduced enthalpy of vaporization of water compared to bulk water ≈2440 J g^{-1}) leading to abundant and consistent water supply and, as a result, the effective solar water evaporation.[40,41] At the same time, upon sun irradiation, the temperature of the system increases, while as shown in Figure 8, a slight temperature increase of NiSe-hyd or CoSe-hyd to 40 °C can cause a marked shift of the $NiSeO_3(H_2O)_2$ related Raman peak at ≈820 cm^{-1} to lower wavenumbers, because of the activation of the hydrated water for transport within the material. Accordingly, the intrinsic absorber nature of these selenite hydrates converts this water to a vapor

state, which results in excellent evaporation rates promising for practical applications.

Using water contaminated with nickel and cobalt poses significant risks to humans due to its toxic and carcinogenic properties. Nickel compounds are categorized by the International Agency for Research on Cancer (IARC) as Carcinogenic Category 1A, indicating they are a proven cause of cancer in humans. Nickel can lead to kidney and lung diseases, chronic asthma, cough, skin dermatitis, allergies, headaches, and lung and nasal cancer, among other health issues.[42] The United States Environmental Protection Agency (USEPA) has set the maximum contaminant level for heavy metals in drinking water within the range of 0.03–800 $\mu g\,L^{-1}$.[43] As was suggested by the World Health Organization (WHO), the maximum admissible limit (MAL) of nickel in drinking water should not exceed 20 $\mu g\,L^{-1}$.[44] According to the MP-AES analysis, the concentration of nickel in the condensed vapor was estimated to be 110 $\mu g\,L^{-1}$, which exceeds MAL from WHO; however, it falls within the range of the recommended level set by the USEPA.

The IARC classifies cobalt and cobalt compounds as "possibly" carcinogenic to humans (Group 2B), meaning that there is sufficient evidence to suggest they cause cancer in animals, but insufficient evidence to establish a causal link in humans. While no epidemiological studies directly link the inhalation of cobalt to lung cancer, chronic exposure to cobalt can lead to respiratory irritation and inflammation such as rhinitis and asthma.[45] WHO does not specify a MAL of cobalt in drinking water. However, New Zealand and the USEPA have estimated maximum allowable levels of cobalt at 1000 and 100 $\mu g\,L^{-1}$, respectively.[46] Based on the MP-AES analysis, cobalt was not detected, indicating that the concentration of cobalt in the collected purified water is below the detection limit of the instrument, specifically less than 15 $\mu g\,L^{-1}$. Therefore, the cobalt selenite hydrate not only exhibited an effective evaporation rate of 2.34 $kg\,m^{-2}\,h^{-1}$ but also ensured the purified water's high purity, entirely free from any metal contaminants.

4. Conclusion

In this study, a new class of inorganic black materials, nickel selenite hydrate and cobalt selenite hydrate, were obtained and synthesized via aqueous method. The main phases in the samples were $NiSeO_3(H_2O)_2$ and $CoSeO_3(H_2O)_2$, respectively, as expected. Both the samples also showed the presence of metallic Se and a negligible amount of $NiSe_2$ and $CoSe_2$. Both the samples were capable of a complete light absorbance in the full solar spectral range, which is a prerequisite to obtain a good candidate for solar water evaporation. By integrating the powders in membrane-based evaporation devices, the high wettability of photothermal membranes in tandem with the continuous water pathway supplied by the cotton stick and the existence of hydrates in the structure enable rapid water supply at the hot surface and, consequently, efficient water evaporation, resulting in evaporation rates of 2.34 and 1.83 $kg\,m^{-2}\,h^{-1}$ for the two materials, which surpass even the values for some hydrophilic absorbers with 3D structure. The high performance in terms of water evaporation can be ascribed to two concurrent processes: 1) the easy water transport through the full device structure and 2) the selective absorption properties of the selenite hydrates, which allows complete absorption of solar radiation and limited re-emission thanks to the low emission properties in the IR region. The possibility to simultaneously optimize light absorption and water transport, at the same time limiting radiative re-emission, indicates a viable and effective strategy to obtain impressive performance in water evaporation. In future investigations, the focus will be on unraveling the intricate mechanisms governing water transportation and identifying the contributing factors responsible for the observed differences in evaporation rates between the distinct compositions of NiSe-hyd and CoSe-hyd. The presence of dissimilar metals in their respective compositions may be responsible for this discrepancy. This will provide valuable insights into the underlying dynamics influencing the performance of these compositions as solar absorbers. With the outstanding vapor generation rates, the nickel and cobalt selenite hydrate compositions show great potential for solar-driven seawater desalination and wastewater purification and represent a simple and elegant way to obtain water desalination through the use of solar radiation.

Acknowledgements

The authors acknowledge Tiziano Finotto and Lorena Gobbo for their technical support with X-Ray diffraction and microwave plasma atomic emission spectroscopy measurements, respectively. I.B.M and E.R.C. thank MICIN/AEI project TED2021-130756B-C31 Next Generation EU. A.V. acknowledges the Kempe Foundation, the Knut & Alice Wallenberg Foundation, for financial support. A.G. and V.M. acknowledge the Project funded by the European Union - NextGenerationEU under the National Recovery and Resilience Plan project IR0000027, CUP: B33C22000710006 - iENTRANCE@ENL: Infrastructure for Energy Transition and Circular Economy @ EuroNanoLab. A.G. and V.M. acknowledge the Project funded by Horizon Europe Grant agreement ID: 101094299 - IMPRESS | Interoperable electron Microscopy Platform for advanced Research and Services. A.V. acknowledges the project funded under the National Recovery and Resilience Plan (NRRP), Mission 4 Component 2 Investment 1.3—Call for tender no. 1561 of 11.10.2022 of Ministero dell'Università e della Ricerca (MUR), funded by the European Union–Next Generation EU Award Number: Project code PE0000021, Concession Decree No. 1561 of 11.10.2022 adopted by Ministero dell'Università e della Ricerca (MUR), CUP D43C22003090001, Project title "Network4 Energy Sustainable Transition—NEST" the Next Generation EU.

Conflict of Interest

The authors declare no conflict of interest.

Data Availability Statement

The data that support the findings of this study are available from the corresponding author upon reasonable request.

Keywords

photothermal conversions, solar hydrate absorbers, solar steam generation, water desalination

Received: March 14, 2024
Revised: May 3, 2024
Published online:

[1] X. Li, J. Li, J. Lu, N. Xu, C. Chen, X. Min, B. Zhu, H. Li, L. Zhou, S. Zhu, T. Zhang, J. Zhu, *Joule* **2018**, *2*, 1331.
[2] D. Xie, M. He, X. Li, J. Sun, J. Luo, Y. Wu, F. Cheng, *Nano Energy* **2022**, *93*, 106802.
[3] H. Li, W. Zhu, M. Li, Y. Li, R. T. K. Kwok, J. W. Y. Lam, L. Wang, D. Wang, B. Z. Tang, *Adv. Mater* **2021**, *33*, 2102258.
[4] Q. Lu, W. Shi, H. Yang, X. Wang, *Adv. Mater* **2020**, *32*, 1.
[5] Z. Liu, Z. Zhou, N. Wu, R. Zhang, B. Zhu, H. Jin, Y. Zhang, M. Zhu, Z. Chen, *ACS Nano* **2021**, *15*, 13007.
[6] A. Taranova, K. Akbar, K. Yusupov, S. You, V. Polewczyk, S. Mauri, E. Balliana, J. Rosen, P. Moras, A. Gradone, V. Morandi, E. Moretti, A. Vomiero, *Nat. Commun.* **2023**, *14*, 7280.
[7] F. Zhao, X. Zhou, Y. Shi, X. Qian, M. Alexander, X. Zhao, S. Mendez, R. Yang, L. Qu, G. Yu, *Nat. Nanotechnol.* **2018**, *13*, 489.
[8] Y. Chen, X. Zhao, Z. Ye, Y. Chen, P. Lin, *Desalination* **2022**, *522*, 115406.
[9] Y. Guo, H. Lu, F. Zhao, X. Zhou, W. Shi, G. Yu, *Adv. Mater* **2020**, *32*, 1.
[10] Y. Guo, X. Zhou, F. Zhao, J. Bae, B. Rosenberger, G. Yu, *ACS Nano* **2019**, *13*, 7913.
[11] Y. Shi, O. Ilic, H. A. Atwater, J. R. Greer, *Nat. Commun.* **2021**, *12*, 1.
[12] Y. Li, X. L. Shi, L. J. Sun, M. Zhao, T. Jiang, W. Jiang, M. Deng, S. Yang, Y. Wang, *Desalination* **2021**, *515*, 115192.
[13] X. Liu, Y. Tian, Y. Wu, F. Chen, Y. Mu, M. L. Minus, Y. Zheng, *ACS Appl. Mater. Interfaces* **2021**, *13*, 42832.
[14] S. Jeong, G. Naidu, R. Vollprecht, T. O. Leiknes, S. Vigneswaran, *Sep. Purif. Technol.* **2016**, *162*, 171.
[15] Q. V. Ly, Y. Hu, J. Li, J. Cho, J. Hur, *Environ. Int.* **2019**, *129*, 164.
[16] E. P. Ng, S. Mintova, *Microporous Mesoporous Mater.* **2008**, *114*, 1.
[17] S. Brunauer, P. H. Emmett, E. Teller, *J. Am. Chem. Soc.* **1938**, *60*, 309.
[18] E. P. Barrett, L. G. Joyner, P. P. Halenda, *J. Am. Chem. Soc.* **1951**, *73*, 373.
[19] Committee D01 *International ASTM Designation: D3359 – 23, ASTM International* **2023**, 1–5.
[20] C. Kennedy, *NREL Tech. Rep.* **2002**, 1.
[21] L. A. Weinstein, J. Loomis, B. Bhatia, D. M. Bierman, E. N. Wang, G. Chen, *Chem. Rev.* **2015**, *115*, 12797.
[22] S. Kim, Z. Tahir, M. U. Rashid, J. I. Jang, Y. S. Kim, *ACS Appl. Mater. Interfaces* **2021**, *13*, 50911.
[23] S. Furuseth, A. Kjekshus, A. F. Andresen, V. Nordal, A. A. Lindberg, J. C. Craig, *Acta Chem. Scand.* **1969**, *23*, 2325.
[24] M. Jia, Y. Jin, P. Zhao, C. Zhao, M. Jia, L. Wang, X. He, *Electrochim. Acta* **2019**, *310*, 230.
[25] A. T. E. Vilian, S. K. Hwang, K. S. Ranjith, M. J. Lee, B. Park, Y. S. Huh, Y. K. Han, *Carbon* **2021**, *178*, 103.
[26] M. Sakthivel, R. Sukanya, S. M. Chen, K. Pandi, K. C. Ho, *Renew. Energy* **2019**, *138*, 139.
[27] H. Liu, H. Guo, N. Wu, W. Yao, R. Xue, M. Wang, W. Yang, *J. Alloys Compd.* **2021**, *856*, 156535.
[28] J. Wang, S. Li, Y. Zhu, S. Zhai, C. Liu, N. Fu, S. Hou, Y. Niu, J. Luo, S. Mu, Y. Huang, *J. Electroanal. Chem.* **2022**, *919*, 116548.
[29] A. B. Mandale, S. Badrinarayanan, S. K. Date, A. P. B. Sinha, *J. Electron. Spectrosc. Relat. Phenom.* **1984**, *33*, 61.
[30] Y. Xu, J. Mo, G. Xie, X. Wang, S. Ding, *J. Mater. Chem. A Mater.* **2020**, *8*, 4457.
[31] Z. Wang, Q. Sha, F. Zhang, J. Pu, W. Zhang, *CrystEngComm* **2013**, *15*, 5928.
[32] Y. Wu, F. Wang, N. Ke, B. Dong, A. Huang, C. Tan, L. Yin, X. Xu, L. Hao, Y. Xian, S. Agathopoulos, *J. Alloys Compd.* **2022**, *925*, 166683.
[33] X. Du, J. Li, K. Tong, X. Zhang, *Dalton Trans.* **2021**, *50*, 6650.
[34] J. Dong, J. Wu, J. Jia, L. Fan, Z. Lan, J. Lin, Y. Wei, *J. Power Sources* **2016**, *336*, 83.
[35] A. Liu, L. Tang, L. Gong, S. Wu, J. Tang, *J. Electroanal. Chem.* **2022**, *923*, 116734.
[36] C. Miao, X. Xiao, Y. Gong, K. Zhu, K. Cheng, K. Ye, J. Yan, D. Cao, G. Wang, P. Xu, *ACS Appl. Mater. Interfaces* **2020**, *12*, 9365.
[37] F. Nie, Z. Li, X. Dai, X. Yin, Y. Gan, Z. Yang, B. Wu, Z. Ren, Y. Cao, W. Song, *Chem. Eng. J.* **2022**, *431*, 134080.
[38] T. P. Gujar, V. R. Shinde, J. W. Park, H. K. Lee, K. D. Jung, O. S. Joo, *Electrochim. Acta* **2008**, *54*, 829.
[39] A. Lukinskas, V. Jasulaitiene, P. Lukinskas, I. Savickaja, P. Kalinauskas, *Electrochim. Acta* **2006**, *51*, 6171.
[40] Y. Chen, J. Yang, L. Zhu, X. Jia, S. Wang, Y. Li, H. Song, *J. Mater. Chem. A Mater.* **2021**, *9*, 15482.
[41] W. Li, X. Li, W. Chang, J. Wu, P. Liu, J. Wang, X. Yao, Z. Z. Yu, *Nano Res.* **2020**, *13*, 3048.
[42] A. Wołowicz, M. Wawrzkiewicz, *Processes* **2021**, *9*, 1.
[43] K. C. Khulbe, T. Matsuura, *Appl. Water Sci.* **2018**, *8*, 1.
[44] M. Vakili, M. Rafatullah, J. Yuan, H. M. Zwain, A. Mojiri, Z. Gholami, F. Gholami, W. Wang, A. S. Giwa, Y. Yu, G. Cagnetta, G. Yu, *Rev. Chem. Eng.* **2021**, *37*, 755.
[45] D. Lison, M. De Boeck, V. Verougstraete, M. Kirsch-Volders, *Occup. Environ. Med.* **2001**, *58*, 619.
[46] G. Mebrahtu, S. Zerabruk, *CNCS, Mekelle Univ.* **2011**, *3*, 105.
[47] H. Wang, R. Zhang, D. Yuan, S. Xu, L. Wang, *Adv. Funct. Mater.* **2020**, *30*, 1.
[48] X. Deng, Y. He, D. Pan, B. Zhang, X. Cui, *Mater. Today Energy* **2022**, *26*, 101016.
[49] X. Fan, Y. Yang, X. Shi, Y. Liu, H. Li, J. Liang, Y. Chen, *Adv. Funct. Mater.* **2020**, *30*, 1.
[50] W. Li, X. Tian, X. Li, J. Liu, C. Li, X. Feng, C. Shu, Z. Z. Yu, *J. Colloid Interface Sci.* **2022**, *606*, 748.
[51] Y. Dong, Y. Lin, C. Du, C. Zhou, S. Yang, *Colloids Surf. A Physicochem. Eng. Asp.* **2022**, *643*, 128755.
[52] Y. Huang, G. Bai, Y. Zhao, Y. Liu, S. Xu, J. Hao, *ACS Appl. Mater. Interfaces* **2021**, *13*, 43094.
[53] D. D. Qin, Y. J. Zhu, R. L. Yang, Z. C. Xiong, *Nanoscale* **2020**, *12*, 6717.
[54] B. Shao, Y. Wang, X. Wu, Y. Lu, X. Yang, G. Y. Chen, G. Owens, H. Xu, *J. Mater. Chem. A Mater.* **2020**, *8*, 11665.
[55] J. Jiang, H. Jiang, Y. Xu, L. Ai, *Desalination* **2022**, *539*, 115977.
[56] D. Ding, H. Wu, X. He, F. Yang, C. Gao, Y. Yin, S. Ding, *J. Mater. Chem. A Mater.* **2021**, *9*, 11241.
[57] H. Jiang, L. Ai, M. Chen, J. Jiang, *ACS Sustain. Chem. Eng.* **2020**, *8*, 10833.
[58] Y. Li, S. Cheng, Z. Yu, R. Gu, Y. Li, H. Chen, *J. Clean. Prod.* **2023**, *392*, 136302.
[59] F. Wang, C. Wang, G. Li, Y. Wang, W. Zhang, G. Shi, X. Yan, J. Shi, *Mater. Today Nano* **2023**, *23*, 100352.
[60] Z. Chen, J. Wang, H. Zhou, Z. Xie, L. Shao, A. Chen, S. B. Wang, S. Bin, N. Jiang, *Adv. Funct. Mater.* **2023**, *33*, 2303656.
[61] Y. Chen, J. Yang, D. Zhang, S. Wang, X. Jia, Y. Li, D. Shao, L. Feng, H. Song, S. Tang, *J. Mater. Chem. A Mater.* **2023**, *11*, 2349.
[62] S. Luo, Z. Liu, X. Yin, Z. Lin, S. Zhang, J. Chen, M. Guo, *Small* **2024**, *20*, 2309087.
[63] W. Wang, Z. Tian, N. He, X. Huan, J. Fan, Y. Li, *Desalination* **2024**, *574*, 117232.
[64] Z. Zhang, X. Wang, G. Li, K. Zhao, G. Liu, Y. Wang, Z. Li, J. Huang, Z. Xu, Y. Lai, X. Qian, S. Zhang, *Chem. Eng. J.* **2024**, *480*, 148006.
[65] Y. Liu, R. S. Sutar, L. Xiang, S. K. Balu, B. Shi, Q. Yang, S. Liu, *New J. Chem.* **2023**, *48*, 1538.
[66] D. Wei, C. Wang, G. Shi, J. Zhang, F. Wang, P. Tan, Z. Zhao, Y. Xie, *Adv. Mater* **2024**, 2309507.